Electronic Supplementary Material (ESI) for CrystEngComm.

Local structure of a switchable dielectric Prussian blue analogue

H. D. Duncan, E. O. R. Beake, H. Y. Playford, M. T. Dove, and A. E. Phillips

Electronic Supplementary Information

Contents

In the following notes, for convenience we refer to the target material of this paper, potassium imidazolium hexacyanoferrate(III), as PIH.

1 Data collection run numbers

The raw data from this experiment are stored in the `ISIS` archive, experiment number 1310322, available at `https://data.isis.stfc.ac.uk`, with run numbers given in Table S1.

Table S1: Collection run numbers for long data sets $> 150\,\mu\mathrm{A\,h}$ for PIH

$T_{\mathrm{nominal}}/\mathrm{K}$	$T_{\mathrm{sample}}/\mathrm{K}$	Run numbers	Total proton beam charge /μA h
293	–	POL62836–POL62843	1200
250	248(2)	POL62917–POL62925	1185
200	194(3)	POL62905–POL62912	1200
180	175(2)	POL62897–POL62904	1200
165	161(3)	POL62889–POL62896	1200
150	146(3)	POL62881–POL62888	1200
83	86(10)	POL62873–POL62880	1200
70	66(3)	POL62872	25
60	59(5)	POL62871	25
50	48(4)	POL62870	25
40	40(5)	POL62869	25
30	31(4)	POL62868	25
20	23(1)	POL62867	25
10	16(7)	POL62859–POL62866	1200

The run numbers for background and normalisation measurements are given in Tables S2 and S3.

Table S2: Run numbers required for normalisation and background corrections for the CCR measurements

Process	Run number	Description	Total proton beam charge /μA h
Normalisation	POL62806–POL62809	8mm V rod	600
Normalisation background	POL62804 POL62805	Empty `POLARIS` changer	300
Sample background	POL62852	Empty `POLARIS` cryostat	600
Container	POL62853, POL62926–POL62928	Empty vanadium can in cryostat	650

Table S3: Run numbers required for normalisation and background corrections for the ambient total scattering measurement

Process	Run number	Description	Total proton beam charge /μA h
Normalisation	POL62806–POL62809	8mm V rod	600
Normalisation background	POL62804 POL62805	Empty `POLARIS` changer	300
Sample background	POL62804–POL62805	Empty `POLARIS` changer	300
Container	POL62810–POL62813	Empty vanadium can in changer	600

2 Data processing

POLARIS has five detector banks, numbered from low to high scattering angle. Of these, detector bank 1 was not used to extract the PDF and scattering functions due to the small Q range it covers. The Q-ranges used for banks 2–5 are given in table S4.

Table S4: Ranges of scattering vector Q used from each detector bank of POLARIS.

Bank	Q_{min} (Å^{-1})	Q_{max} (Å^{-1})
2	0.30	4.55
3	0.80	4.55
4	2.09	46.00
5	3.37	46.00

The decision where to place the Q cutoffs for each bank was based on how well the differential cross sections for the individual banks merged to produce the final differential cross section and the agreement between the observed and expected PDFs. To perform the latter comparison, the cumulative PDF integral $C(r) = \int_0^r G'(\rho)d\rho$ was calculated in the range $r \leq 2.25\,\text{Å}$ for the expected molecular geometry and for the experimental data (Fig. S1). We found that best agreement was obtained when the range of the low-angle banks was limited such that they only contributed to the low-Q region of the scattering data. This minimises the errors associated with inelastic scattering, especially from the light deuterium atoms. After adjustment of the Q range, good agreement was observed between the expected and GUDRUN-derived cumulative sum of this well-understood region, with the sole exception that the area under the peak at $r = 1.05\,\text{Å}$ (corresponding to the C$-$D and N$-$D bonding pairs) was slightly too small to account for the known coordination number.

One obvious explanation for this disagreement would be that our sample was not fully deuterated. However, allowing the deuteration fraction to refine in Rietveld analysis did not give a better fit or a refined value less than 100%, nor was there any sign of the strong incoherent scattering one would expect from ^{1}H. We conclude, therefore, that the deuteration fraction is not the reason for this discrepancy and that our sample was indeed fully deuterated.

After the bank cut-offs had been chosen, the "tweak factor" (roughly, the reciprocal packing fraction) was adjusted so that the high Q value of the merged differential cross section matched the expected level, $\sum_i c_i b_i$, where c is the atom fraction and b the neutron scattering length. Termination ripples due to a finite Q range were smoothed using the modified Lorch function provided in GUDRUN, with width given by

$$\Delta(r) = (0.02\,\text{Å})(1 + r^{\beta}).$$

Values of the tweak factor and β are given for each temperature in table S5.

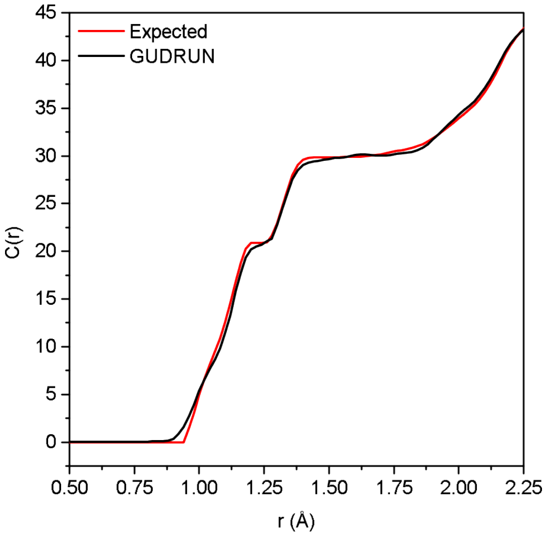

Figure S1: Cumulative integral $C(r)$ as observed and expected for $r \leq 2.25\,\text{Å}$ after optimisation of the individual bank cutoffs in GUDRUN.

Table S5: Smoothing parameter β and `GUDRUN` "tweak" factor used when processing the PDFs

Nominal temperature	β	Tweak factor
293	2.4498	0.5345
250	2.9026	0.5320
200	2.9009	0.5592
180	2.8934	0.5229
165	2.8934	0.4878
150	2.8934	0.5170
83	2.5889	0.5195
10	2.6140	0.5434

3 Restraints applied to refinements

Restraints were applied during both Rietveld and RMC refinements to maintain chemically plausible geometries of the polyatomic ions, while allowing the framework geometry to refine freely. In both Rietveld and RMC refinements, intramolecular bonds and angles were restrained. In the RMC refinement, the atoms of the imidazolate ion were also restrained to lie in a plane by the addition of a penalty term equal to $C\sum_j d_j^2$, where d is the distance of an atom from the best-fit plane and $C = 5000\,\mathrm{eV\,\AA}^{-2}$. In addition, "distance windows" were applied during RMC refinement such that atom pairs that are within the given window in the starting configuration are not allowed to leave it.

The potentials used were chosen based on the standard MM3 potential set; our results are not sensitive to small variations in these potentials. The numerical values of these potentials and distance windows are provided in tables S6, S7, S8 and S9 below.

Table S6: Bond types and restraints applied to the $C2/c$ `GSAS` (Rietveld) refinement.

Bond type	Restraint length /Å
Fe–C	1.940
K–N	2.860
C–N* (cyanide)	1.150
C–D	1.030
N–D	1.030
C–C	1.270
C–N (N–C–N)	1.285
C–N (C–C–N)	1.370

* applied to the $R\bar{3}m$ refinement as well

Table S7: Morse bond stretch potentials used to constrain RMC refinement, according to the penalty term $E = D(1-\exp\{-\alpha(r-r_0)\})^2$. We set $\alpha = 2.55\,\mathrm{\AA}^{-1}$ throughout, in accordance with the MM3 potential set. Cx and Nx correspond to cyanide atoms in the framework which need to be differentiated from the C and N of the imidazole ring.

Atomic pair	D/eV	$r_0/\mathrm{\AA}$
C−C	3.600	1.34
C−D	2.472	1.04
C−N	4.821	1.34
N−D	2.928	1.03
Cx−Nx	8.317	1.16

Table S8: Angle potentials used to constrain RMC refinement, according to the penalty term $E = \frac{1}{2}k(\cos\theta - \cos\theta_0)^2$.

Atoms	k/eV	θ_0/°
D−C−N	6.429	126.0
C−N−D	7.2405	126.0
N−C−N	4.993	126.0
C−N−C	10.174	118.3
C−C−N	10.174	120.0
C−C−D	6.117	126.0

Table S9: Distance windows applied to RMC refinements.

T/K	D−C	D−N	C−C	C−N	Cx−Fe	Cx−Nx	K−Nx
293	0.93-1.15	0.93-1.15	1.25-1.46	1.25-1.46	1.82-2.07	1.08-1.26	2.60-3.18
250	0.93-1.15	0.93-1.15	1.25-1.46	1.25-1.47	1.83-2.09	1.10-1.23	2.58-3.16
200	0.93-1.15	0.93-1.16	1.25-1.47	1.25-1.47	1.83-2.09	1.10-1.23	2.57-3.16
180	0.93-1.16	0.93-1.12	1.25-1.47	1.25-1.47	1.83-2.09	1.10-1.23	2.57-3.16
165	0.93-1.16	0.93-1.16	1.26-1.47	1.25-1.47	1.83-2.09	1.10-1.23	2.57-3.16
150	0.92-1.15	0.90-1.14	1.22-1.41	1.22-1.45	1.83-2.12	1.07-1.22	2.56-3.19
83	0.93-1.16	0.92-1.15	1.21-1.40	1.21-1.45	1.84-2.10	1.09-1.21	2.57-3.17
10	0.88-1.13	0.86-1.15	1.23-1.42	1.24-1.46	1.84-2.10	1.09-1.24	2.53-3.17

4 Convergence criteria

Representative convergence plots for the three data sets models were refined against are given in figure S2. RMC was run for four days for each configuration, corresponding to approximately 4.5×10^6 accepted atomic moves in the high- and intermediate-temperature phase and 6.4×10^6 accepted atomic moves in the low-temperature phase.

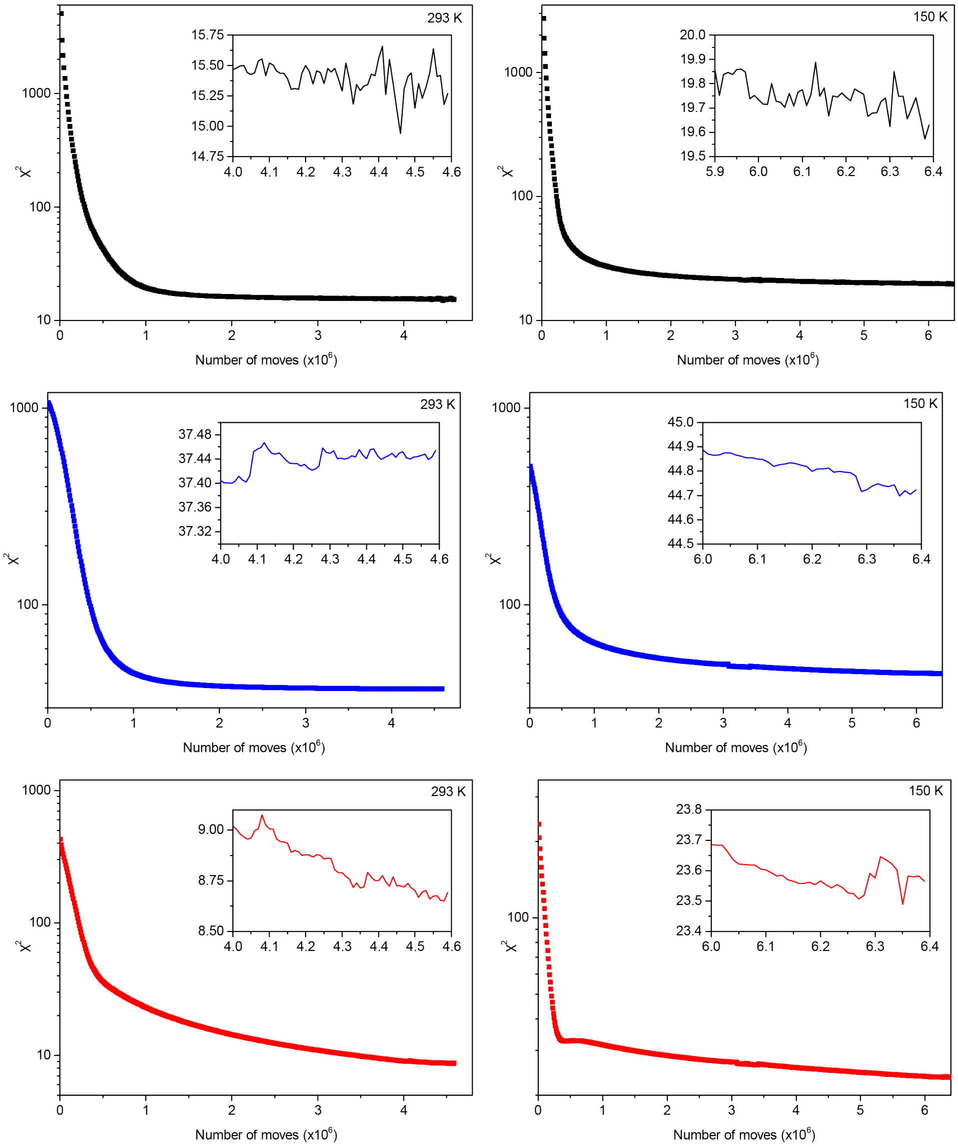

Figure S2: Evolution of χ^2 with number of accepted atomic moves for PIH model at $293\,\mathrm{K}$ (left) and $150\,\mathrm{K}$ (right). The χ^2 component from $D(r)$ is shown in black, Bragg in blue, and $i(Q)$ in red.

5 Representative fits

Representative fits for $D(r)$ in the intermediate- and low-temperature phases are given in figure S3.

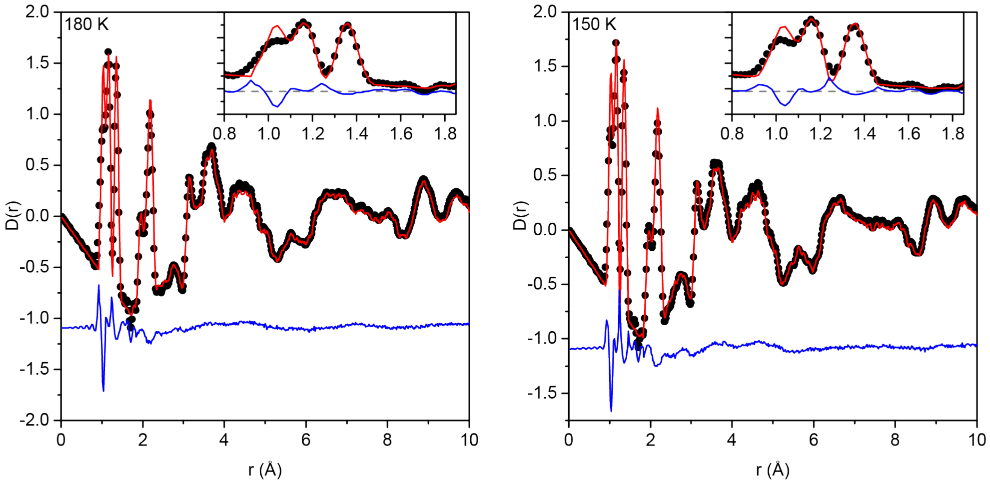

Figure S3: Left: The observed (black dots) and calculated (red line) $D(r)$ for an intermediate-temperature phase refinement with the offset difference in blue for $r = 0\,\text{Å}$ to $10\,\text{Å}$. Insert shows the low-r peaks. Right: the corresponding plot for a low-temperature phase refinement.

6 Polyhedral deformation

The angles made within the KN_6 and FeC_6 polyhedra in the high- intermediate- and low-temperature phase configurations were extracted. For all phases the more ionic KN_6 octahedra displayed a wider distribution of angles than the more covalent FeC_6 octahedra. Both the K-centered and Fe-centered polyhedra displayed a regular distribution of angles which confirms that the polyhedra are not substantially distorted in any phase.

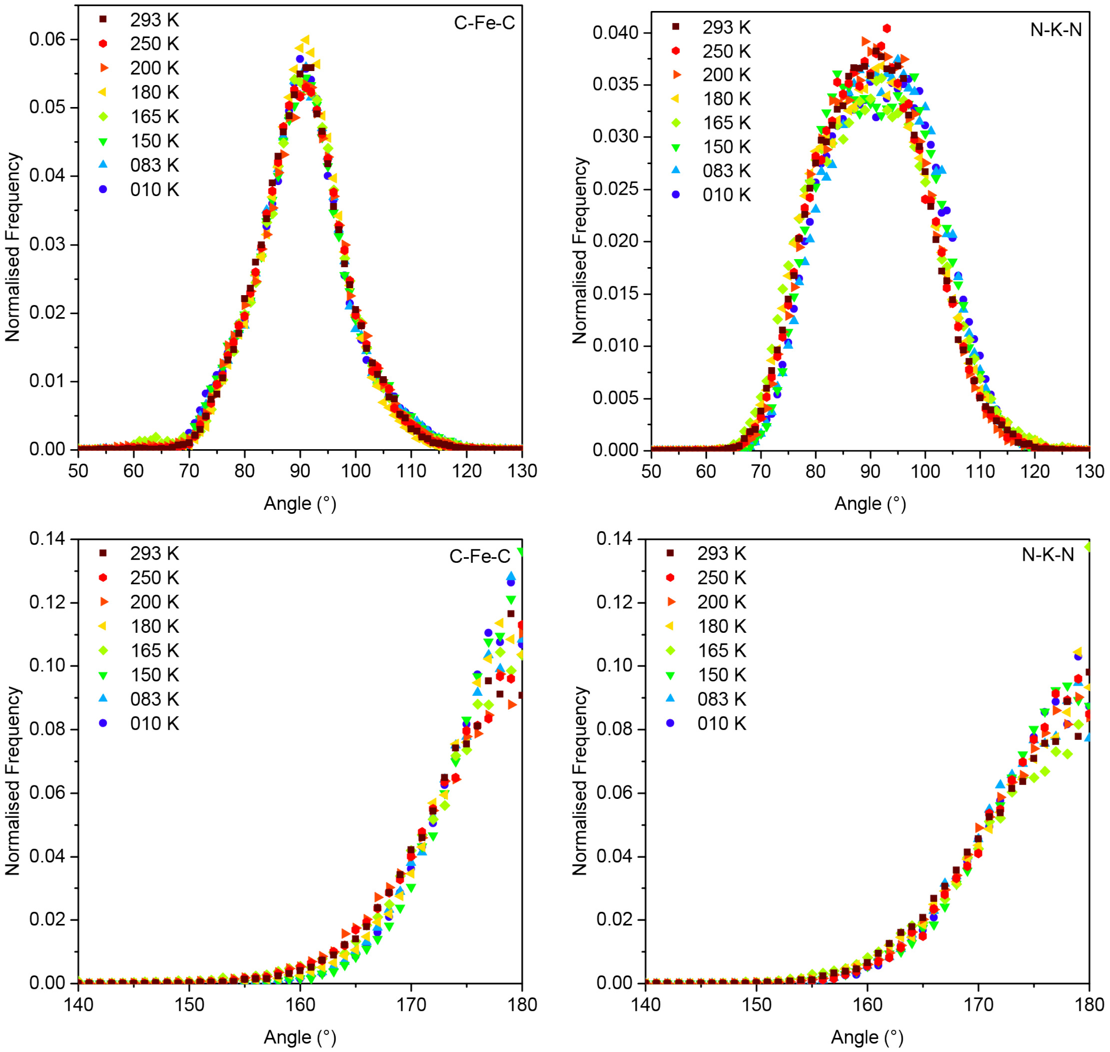

Figure S4: The distribution of N−K−N and C−Fe−C angles. Top row: All angles $\approx 90^\circ$ for the FeC$_6$ and KN$_6$ polyhedra (left and right respectively). Bottom row: All angles $\approx 180^\circ$ for the FeC$_6$ and KN$_6$ polyhedra (left and right respectively)

7 Centroid–framework partial PDFs

The partial PDF for the centroid–cyanide C atom distances, analogous to Figure 4(a) in the paper, is given in figure S5. In the low-temperature phase both partial PDFs display a bimodal distribution, with the centroid–N distribution showing a continuous change and the centroid–C distribution a more abrupt change between the electrically disordered and ordered phases. This might be expected since the C atoms are closer to the centre of the relatively rigid hexacyanoferrate ions, and their motion will therefore be dominated by the rotation of these ions associated with the order-disorder phase transition. In neither graph is there any indication of anomalous behaviour between the intermediate- and high-temperature phases.

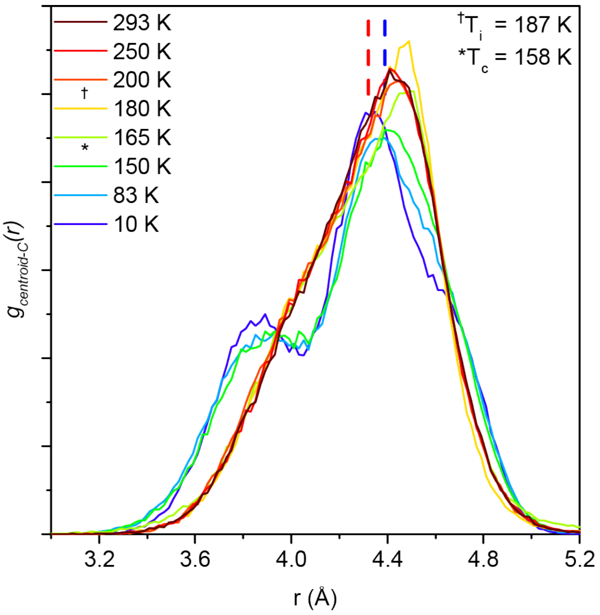

Figure S5: Partial pair distribution functions from the centre of the imidazolium to the cyanide C atoms of the framework. Dashed lines indicate the initial centroid···C distances for the high and intermediate-temperature phases (red) and low-temperature phase (blue).

8 Metal–cyanide angle distributions

The average metal–cyanide angles Fe—C—N (brown) and K—N—C (purple) from Rietveld analysis are shown in figure S6. Like the corresponding RMC data in the main paper, these results show that the ionic K-centred environments are more distorted and accommodate smaller angles than the more covalent Fe-centred environments. Since both the high- and intermediate-temperature phases have $R\bar{3}m$ symmetry, there is no observable difference between the high- and intermediate-temperature phases.

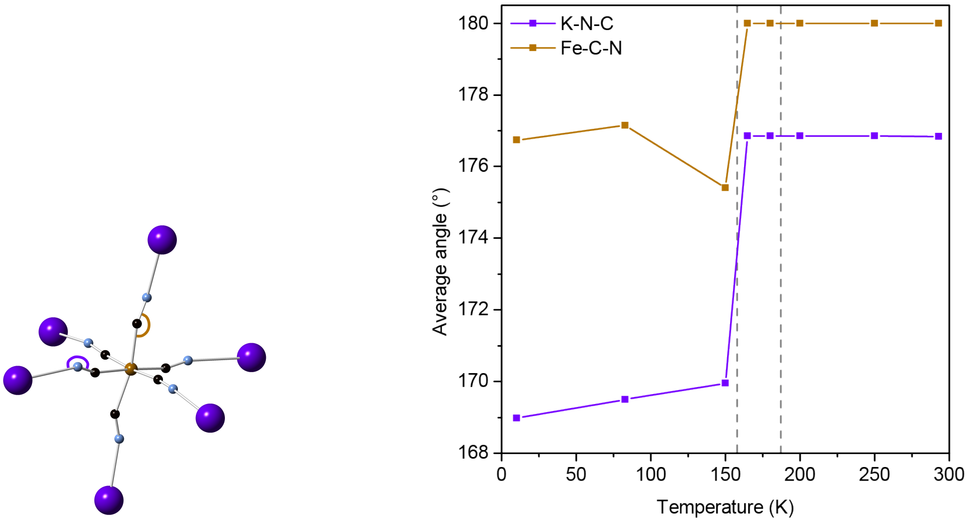

Figure S6: Left: Octahedral coordination for $\mathrm{Fe(CNK)_6}$ from a 293 K refined atomistic configuration. The Fe—C—N angle is shown in brown, and the K—N—C in purple. Right: Rietveld-derived average angles Fe—C—N (brown) and K—N—C (purple).

The Fe—C—N angles from RMC analysis (again normalised by $\sin\theta$ to correct for the variation in solid angle with θ) and corresponding Gaussian fits are shown in figure S7, analogous to Figure 3(c) in the main paper. Dashed lines show the angles from the Rietveld (average) structure in the high- and low-temperature phases.

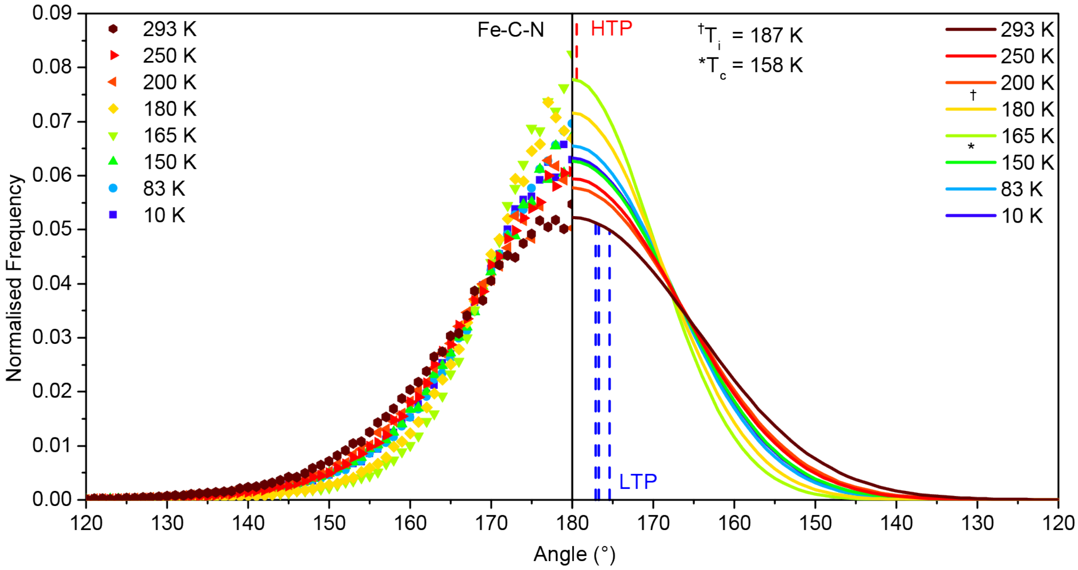

Figure S7: Distribution of Fe−C−N angles. Left: RMC data. Right: Gaussian fit. Like the K−N−C data in the main paper, the distribution of angles is much sharper in the intermediate temperature phase. Dashed lines indicate the corresponding angles from the average structure for the high and low temperature phases.

9 Lattice parameters

The lattice parameters for the high and low temperature phases obtained from Rietveld refinement, expressed in terms of the $C2/c$ cell, are given in Table S10 below:

Table S10: Lattice parameters in terms of the $C2/c$ cell

$T_{\mathrm{nominal}}/\mathrm{K}$	$a/\mathrm{Å}$	$b/\mathrm{Å}$	$c/\mathrm{Å}$	$\beta/^{\circ}$	Volume / $\mathrm{Å}^3$
293	13.6906(7)	8.7570(4)	15.1675(4)	111.6720(2)	1689.87(19)
250	13.6518(5)	8.7631(3)	15.1782(3)	111.7528(2)	1686.49(14)
200	13.5944(9)	8.7695(6)	15.1892(6)	111.8661(3)	1680.5(3)
180	13.5610(6)	8.7749(3)	15.1985(3)	111.9369(2)	1677.61(15)
165	13.5271(6)	8.7820(3)	15.2109(3)	112.0135(2)	1675.24(15)
150	13.4932(4)	8.7830(4)	15.1048(6)	111.6565(35)	1663.73(12)
83	13.4535(4)	8.7911(3)	15.0805(5)	111.7453(30)	1656.67(10)
70	13.4400(5)	8.7912(6)	15.0750(9)	111.771(5)	1654.12(11)
60	13.4356(5)	8.7914(6)	15.0732(10)	111.779(5)	1653.32(12)
50	13.4306(6)	8.7913(6)	15.0721(10)	111.792(5)	1652.42(13)
40	13.4261(4)	8.7928(5)	15.0671(8)	111.799(4)	1651.52(10)
30	13.4229(5)	8.7936(5)	15.0664(8)	111.802(4)	1651.16(10)
20	13.4206(5)	8.7934(5)	15.0655(8)	111.805(4)	1650.72(11)
10	13.4212(6)	8.7934(4)	15.0633(8)	111.8038(27)	1650.56(14)

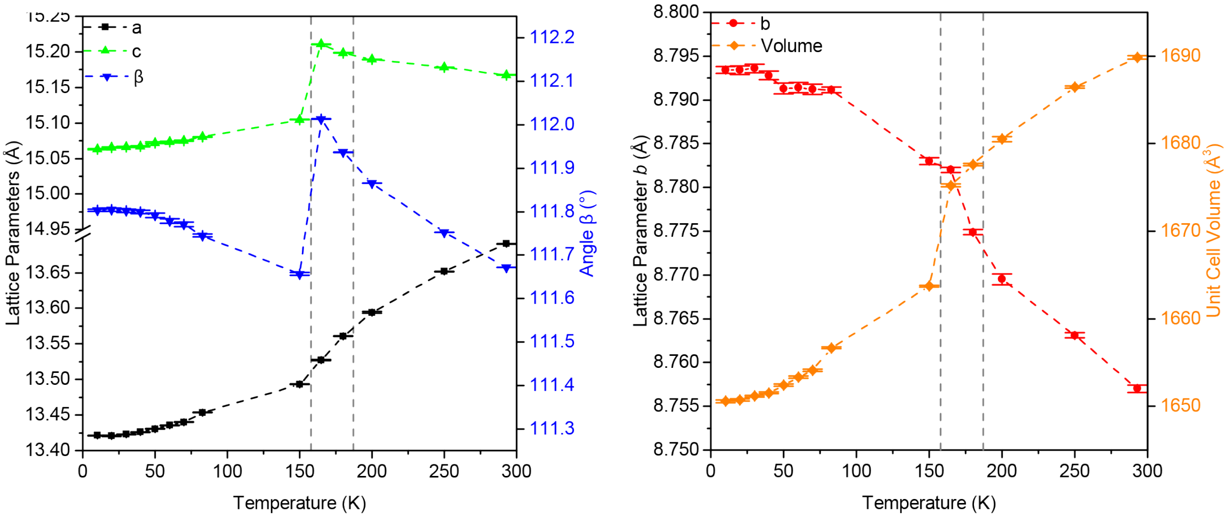

Figure S8: Left: Lattice parameters a, c, and β through the high, intermediate, and low-temperature phases. Right: the b lattice parameter and calculated unit cell volume. Unlike all the other parameters, there is a contraction along the b axis on heating. Data includes short $25\,\mu\mathrm{A\,h}$ runs between $10\,\mathrm{K}$ and $83\,\mathrm{K}$.

10 Strain analysis

The lattice parameters of PIH (expressed in terms of the $C2/c$ unit cell) were extrapolated linearly and used to calculate the Eulerian strain tensor. The resulting principal components are plotted in Fig. S9.

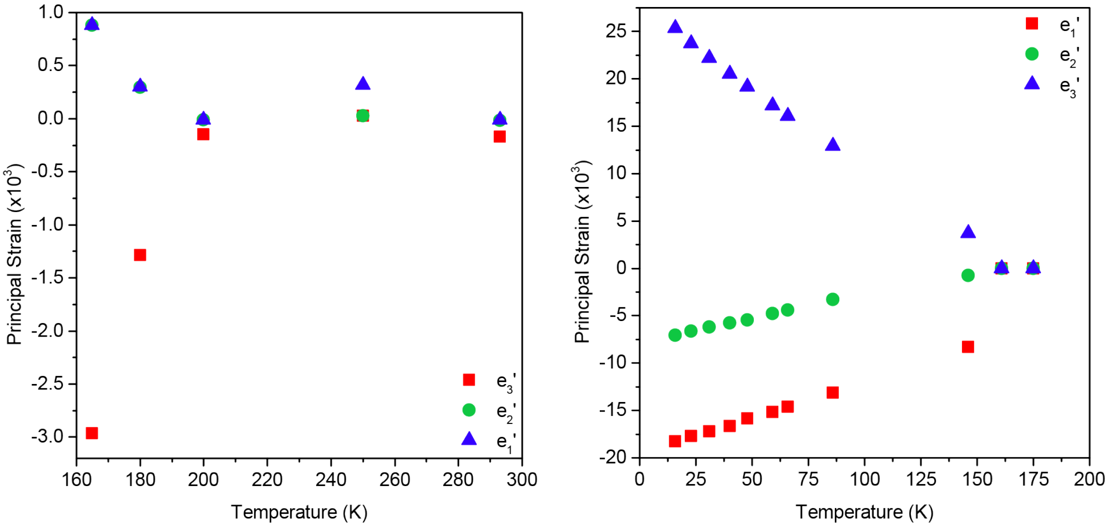

Figure S9: Left: Principal components of the strain tensor for the high to intermediate temperature phases. Right: Principal components of the strain tensor for the intermediate to low temperature phase. The phase change at 158 K shows significantly more change in the components than 187 K transition.